# Quantitative SPECT Reconstruction of Iodine-123 Data

David R. Gilland, Ronald J. Jaszczak, Kim L. Greer, R. Edward Coleman

*Department of Radiology, Duke University Medical Center, Durham, North Carolina*

Many clinical and research studies in nuclear medicine require quantitation of iodine-123 ($^{123}$I) distribution for the determination of kinetics or localization. The objective of this study was to implement several reconstruction methods designed for single-photon emission computed tomography (SPECT) using $^{123}$I and to evaluate their performance in terms of quantitative accuracy, image artifacts, and noise. The methods consisted of four attenuation and scatter compensation schemes incorporated into both the filtered backprojection/Chang (FBP) and maximum likelihood-expectation maximization (ML-EM) reconstruction algorithms. The methods were evaluated on data acquired of a phantom containing a hot sphere of $^{123}$I activity in a lower level background $^{123}$I distribution and nonuniform density media. For both reconstruction algorithms, nonuniform attenuation compensation combined with either scatter subtraction or Metz filtering produced images that were quantitatively accurate to within 15% of the true value. The ML-EM algorithm demonstrated quantitative accuracy comparable to FBP and smaller relative noise magnitude for all compensation schemes.

**J Nucl Med 1991; 32:527–533**

Iodine-123 ($^{123}$I) has chemical and physical properties that are appropriate for radiolabeling and imaging many pharmaceuticals. Quantitation of the distribution of $^{123}$I is important for determining the kinetics and dosimetry of these tracers (*1, 2*). While the quantitative capability of single-photon emission computed tomography (SPECT) with technetium-99m ($^{99m}$Tc) has been studied extensively (*3, 4*), with few exceptions (*5–14*) there has been relatively little investigation into the quantitative capability of SPECT with $^{123}$I. For the lack of a better method, conjugate view, planar techniques (*1, 15*) have been used to obtain quantitative information. This work explored the quantitative potential of SPECT with $^{123}$I.

Received Jun. 1, 1990; revision accepted Aug. 21, 1990.
For reprints contact: David R. Gilland, Ph D, Box 3949, Department of Radiology, Duke University Medical Center, Durham, North Carolina 27710.

This study used $^{123}$I (p,5n) in order to reduce $^{124}$I contamination more prevalent in $^{123}$I (p,2n). This contaminant has been found to render low-energy collimators unsuitable for planar imaging with $^{123}$I (p,2n) (*12*). The high energy emissions of $^{124}$I (>500 keV) penetrate the collimator septa and degrade the quality of the acquired data. Additional processing is often required when there is a significant level (>5%) of septal penetration.

The major impediments to SPECT quantitation with $^{123}$I are the same as with $^{99m}$Tc: attenuation, scatter, finite spatial resolution, and image noise. Compensation of $^{99m}$Tc data for these effects is often incorporated into the SPECT reconstruction algorithm. With $^{123}$I data, however, these standard compensation techniques may be quantitatively inaccurate due to differences in energy spectra between the two radioisotopes. The objective of this study was to implement several SPECT reconstruction methods designed for $^{123}$I data and to evaluate their performance in terms of quantitative accuracy, image artifacts, and noise.

Four attenuation and scatter compensation schemes were incorporated into both the filtered backprojection/Chang (FBP) reconstruction algorithm (*16*) and maximum likelihood-expectation maximization (ML-EM) algorithm (*17–19*). The Chang algorithm is a modification of the conventional filtered backprojection algorithm which allows compensation for attenuation. Thus, the FBP/Chang algorithm is based on an analytical solution to the reconstruction problem. The ML-EM method takes a statistical approach and considers the emissions from a source voxel as a random Poisson process. The iterative ML-EM algorithm successively estimates the means of these processes and can be stopped after a specified number of iterations. Both of these algorithms perform attenuation compensation after specification of an attenuation coefficient distribution within the reconstruction plane.

This study examined the relative merit of uniform versus nonuniform attenuation compensation. The conventional approach is to assume uniform attenuation within a body boundary that can be determined from an uncorrected reconstruction (*20*), a reconstruction of transmission or scatter data (*21*), or camera

orbit information. Other investigators have demonstrated improved image quality with $^{99m}$Tc (*22*) and $^{201}$Tl data (*23*) when nonuniform attenuation compensation is incorporated in the reconstruction. Nonuniform attenuation information is more difficult to obtain since a transmission study using a gamma-emitting source is required (*24*). The advantage of nonuniform over uniform attenuation compensation will be more pronounced in body regions of nonuniform tissue density such as the thorax.

Three methods of scatter compensation were evaluated in this study. These included broad-beam attenuation compensation (*4*), scatter subtraction (*25*), and scatter deconvolution by Metz filter (*26*). The broad-beam approach compensates for scatter, in effect, by under-correcting for attenuation. The broad-beam attenuation coefficients depend on the source geometry and are less than narrow beam due to detection of scatter events. With the scatter subtraction technique, the scaled data acquired in an energy window below the photopeak window are subtracted from the photopeak data before reconstruction. This technique is based on the assumption that a fixed fraction of the scatter energy window data adequately approximates the scatter component of the photopeak data. The Metz filter is a deconvolution filter at low spatial frequencies, where the signal-to-noise ratio is greatest, and approaches zero gain at higher frequencies where noise dominates the signal. Scatter compensation is achieved by deconvolution of the scatter response. The deconvolution technique makes the approximation of a shift-invariant system response.

## METHODS

The reconstruction methods were evaluated in a phantom study. The phantom consisted of plastic cylinder of elliptical cross section containing low-density wood "lungs," nylon "spine," and a hollow, plastic sphere (Fig. 1). In the axial dimension, perpendicular to the elliptical cross section, the cylinder was 24 cm long. The lungs and the spine extended the total axial length of the cylinder. In cross section, the lungs were 8.8 × 10 cm, and the spine was 2.5 × 2.5 cm. The sphere was 3.5 cm in diameter. The inside of the cylinder, or background, and the inside of the sphere were filled with $^{123}$I sodium iodide solution at concentrations of 1.3 and 6.7 $\mu$Ci/ml, respectively. The concentrations were determined from planar camera measurements of 20 cc syringes containing samples of each solution and from the known sensitivity of the camera/collimator.

Projection images were acquired using a three-headed SPECT system with medium-energy collimators (Trionix Research Laboratories). The projections were acquired in a 128 × 128 matrix with a pixel size of 3.56 mm. There were 120 projection angles equally spaced over 360°. The total scan time was 20 min. The photopeak energy window was 20% in width and centered at 159 keV, the primary emission energy of $^{123}$I. The scatter energy window ranged from 100 to 140 keV. Standard camera uniformity correction was performed.

A total of eight reconstruction methods were evaluated including four compensation schemes implemented within both the filtered backprojection algorithm with single iteration Chang compensation (FBP) and the ML-EM algorithm. The eight methods are described in Table 1. The methods were chosen in order to investigate the relative merits of FBP/Chang versus ML-EM reconstruction, uniform versus nonuniform attenuation compensation, and scatter compensation by broad-beam attenuation map versus scatter subtraction versus Metz filtering.

The Chang compensation method was used in its single iteration form and generalized for nonuniform attenuation. In this form, each pixel in the initial filtered backprojection reconstruction is multiplied by a correction term which is related to the average attenuation for that pixel. Thus, the correction term for pixel i, j can be written as:

$$C(i,j) = \frac{1}{\frac{1}{M}\sum_{m=1}^{M} \exp\left[-\sum_{i' \in I_{ijm}} \sum_{j' \in J_{ijm}} \mu(i',j')d(i',j',m)\right]}, \quad (1)$$

where M is the number of angles, $I_{ijm}$ and $J_{ijm}$ are the set of i and j indices, respectively, of pixels intersected along the path to the detector at angle m, $\mu(i, j)$ is the attenuation coefficient distribution, and d(i, j, m) is the path length through pixel i, j at angle m. This first-order corrected image is then reprojected in a way that models attenuation (*27*) based on the specified attenuation coefficient distribution. The reprojection is subtracted from the original measured data to generate error projections. An error image is then reconstructed by filtered backprojection and each pixel in the error image is multiplied

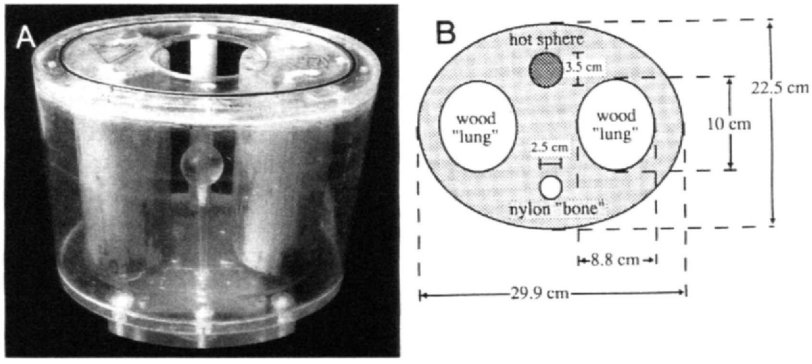


**FIGURE 1**
(A) Photograph of experimental phantom showing sphere in foreground, "spine" in background, and wood "lungs." (B) Sketch of experimental phantom giving dimensions of sphere, spine, lungs, and cylinder.

**TABLE 1**
Reconstruction Methods

| Method name | Recon. algorithm | Attenuation map* | Scatter sub. (S) or Metz filter (M) |
|---|---|---|---|
| FBU | FBP | U/broad | |
| FBN | FBP | N/broad | |
| FBS | FBP | N/narrow | S |
| FBM | FBP | N/broad | M |
| MLU | ML-EM | U/broad | |
| MLN | ML-EM | N/broad | |
| MLS | ML-EM | N/narrow | S |
| MLM | ML-EM | N/broad | M |

* U = uniform attenuation map; N = nonuniform attenuation map; broad=broad-beam attenuation coefficients; and narrow=narrow-beam attenuation coefficients.

by the corresponding correction term. The error image is then added to the first-order corrected image to generate the single iteration image. The filter used for these filtered backprojection reconstructions was a ramp function to the Nyquist frequency. (The Nyquist frequency is equal to $1/(2d)$ where d is the linear sampling interval. For this study, therefore, the Nyquist frequency was equal to 1.40 cycles/cm).

In this implementation of the ML-EM algorithm, the projector and backprojector modeled attenuation (*27*) using the specified attenuation coefficient distribution. The initial estimate was a uniform distribution, and the algorithm was stopped after 50 iterations. This iteration stopping point was selected after examining reconstructions at 25, 50, and 100 iterations using nonuniform, broad-beam attenuation compensation. The differences in the quantitative level in the sphere and background regions at the three iteration stopping points were negligible. However, the level in the lungs was reduced 30% from 25 to 50 iterations but only 12% from 50 to 100 iterations. Noise, measured by the standard deviation of pixel intensities within an region of interest (ROI) in the background region, increased 38% from 25 to 50 iterations and 34% from 50 to 100 iterations. Because from 25 to 50 iterations there was significant gain in accuracy in the lung regions while from 50 to 100 iterations there was only a mild gain in accuracy in the same regions and noise continued to worsen, 50 iterations was chosen as the stopping point.

The uniform and nonuniform attenuation maps used by all methods were computer-simulated based on the known phantom dimensions and attenuation coefficients. The attenuation coefficients used for the nonuniform, narrow-beam attenuation map were 0.17 $cm^{-1}$ for nylon, 0.14 $cm^{-1}$ for water, and 0.01 $cm^{-1}$ for wood. The broad-beam attenuation coefficient for water, 0.10 $cm^{-1}$, was determined empirically for the case of the elliptical cylinder filled uniformly with $^{123}I$ in water. The broad-beam value for nylon, 0.12 $cm^{-1}$, was obtained by scaling the narrow-beam value for nylon by 0.71, the ratio of broad-to-narrow beam coefficient for water. Because of minimal scatter in the wood, the broad-beam value was set equal to the narrow-beam value.

The constant attenuation coefficient in the uniform attenuation map was computed as the average of the attenuation coefficients within the elliptical body in the nonuniform, broad-beam attenuation map. All attenuation maps were filtered with a Hanning filter (*4*) at a cut-off frequency equal to the Nyquist in order to minimize the effects of any possible misregistration of the attenuation map and the data. The narrow-beam, nonuniform attenuation map is illustrated in Figure 2.

The scatter subtraction technique subtracts from the photopeak energy window data, $Y_{photopeak}$, a fixed fraction, k, of the scatter energy window data, $Y_{scatter}$. Thus, the scatter compensated data can be expressed:

$$Y_{corrected} = Y_{photopeak} - k*(Y_{scatter}). \quad (2)$$

Determining the optimal value for k requires an empirical approach since this value will likely depend on the source and attenuation distributions, the energy resolution of the imaging system, and the energy window settings (*25*). For this investigation the value of k was chosen so that the average counts in the lung areas was zero when the first-order Chang algorithm is used to reconstruct the scatter subtracted phantom data. The rationale for this criterion is based on the experimental finding that the lacquered wood "lungs" of this phantom do not absorb radioactivity during immersion, and therefore the true counts in the lung areas was zero. For our system and energy window settings, the value of k which resulted in zero count density in the lung areas of the first-order Chang reconstruction was 0.4.

The Metz filter used in this study is defined in the frequency domain as:

$$M(\upsilon) = \frac{1 - (1 - MTF^2(\upsilon))^X}{MTF(\upsilon)}, \quad (3)$$

where $MTF(\upsilon)$ is an estimate of the system modulation transfer function. The parameter X controls the extent of the deconvolution; at larger values of the parameter the filter follows the inverse MTF to higher frequencies. For this study, X was set equal to five. Effort was not taken to determine the optimal value for X. The optimal value will depend in a complicated way on the count level, image structure and system MTF (*28, 29*) as well as the performance criterion. A value of five for X results in a conservative degree of deconvolution. The MTF for this study was approximated as the product of a geometric collimator response function and a series-equivalent scatter response function. By incorporating the scatter response into the MTF, the Metz filter provided compensation for scatter. The collimator response function

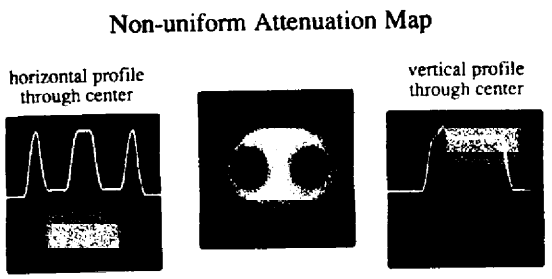


Attenuation map used for nonuniform attenuation compensation is shown in the center along with horizontal and vertical profiles through the center of the map.

was based on line source measurements in air with the medium-energy collimator and a source-to-detector distance of 10 cm. The series-equivalent scatter response function was based on Monte Carlo simulations of a point source located 8 cm deep in a water bath. The Metz filter used in the study is plotted in Figure 3.

The absolute quantitative accuracy of the eight methods was evaluated in the sphere, background, and lung regions. Count densities were measured in these regions of the reconstructed images using a five-pixel ROI located in the center of the sphere and 20-pixel ROIs located in the center of each lung and in the background region between the lungs. From the count densities, the $^{123}I$ concentrations ($\mu$Ci/ml) were computed based on the measured sensitivity of the SPECT system with medium-energy collimators. The "true" concentration of each solution was base on planar camera measurements of 20-cc samples contained in a syringe and the measured camera sensitivity. As a measure of noise level, the relative noise magnitude, defined as the standard deviation of pixel intensities divided by the mean, was computed for each reconstruction method for the ROI located in the background region. In addition, profiles were drawn through the reconstructed images to further illustrate the noise level and quantitative accuracy of the reconstruction methods.

## RESULTS

The results of the quantitative analysis for the eight reconstruction methods are summarized in Table 2. The filtered backprojection method without compensation (FB) has been included for reference using similar ROI measurements. The ratio of the reconstructed $^{123}I$ concentration to the true concentration for the sphere and background regions is given in columns 2 and 3, respectively. Column 4 gives the reconstructed concentration in the lung areas where there was actually no $^{123}I$ present.

The results presented in Table 2 reveal a number of important characteristics of these reconstruction methods in terms of quantitative accuracy. First, there is dramatic improvement in both the FBP/Chang and ML-EM methods with the incorporation of nonuniform attenuation information (FBN and MLN). This

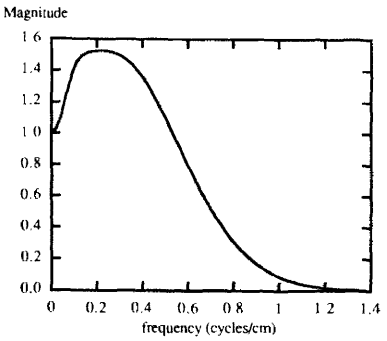


**FIGURE 3**
Metz filter used for scatter deconvolution. The scatter response function is incorporated into the MTF in the filter formulation.

**TABLE 2**
Quantitation and Noise Analysis

| Recon. method* | R† | | μCi/ml in lungs‡ | Relative noise magnitude§ |
|---|---|---|---|---|
| | Sphere | Bckgrd | | |
| FB | 0.28 | 0.27 | 0.17 | 0.317 |
| FBU | 0.69 | 0.74 | 0.33 | 0.219 |
| FBN | 0.76 | 0.94 | 0.12 | 0.165 |
| FBS | 0.94 | 0.88 | 0 | 0.254 |
| FBM | 1.02 | 0.91 | −0.02 | 0.150 |
| MLU | 0.69 | 0.68 | 0.52 | 0.175 |
| MLN | 0.78 | 0.91 | 0.11 | 0.144 |
| MLS | 0.98 | 0.90 | 0.03 | 0.207 |
| MLM | 1.06 | 0.97 | −0.06 | 0.106 |

* See Table 1 for description of methods.
† R = ratio of reconstructed μCi/ml to true μCi/ml.
‡ True μCi/ml in lungs = 0.
§ Standard deviation divided by the mean of pixel intensities within an ROI located in the background region.

confirms previous results with $^{99m}Tc$ data (*22*) and $^{201}Tl$ data (*23*). Second, with uniform attenuation compensation (FBU and MLU), the counts in the lung areas were relatively high and in the sphere and background areas inaccurately low. This effect can be further appreciated in Figures 4 and 5 which show the reconstructions with FBP/Chang and ML-EM, respectively, with both uniform and nonuniform attenuation compensation. The profiles through the images illustrate the reduction of counts in the lung areas with nonuniform compensation.

While nonuniform, broad-beam compensation improved the quantitative accuracy over uniform compensation, there was still a significant count level in the lungs and the levels in the sphere and background were too low. The scatter subtraction techniques (FBS and MLS), however, reduced the counts in the lung areas to negligible levels and improved the accuracy in the sphere and background regions. (Since the value of k was chosen so that the first-order Chang reconstruction with scatter subtraction would have zero count density in the lung regions, it is not surprising that single

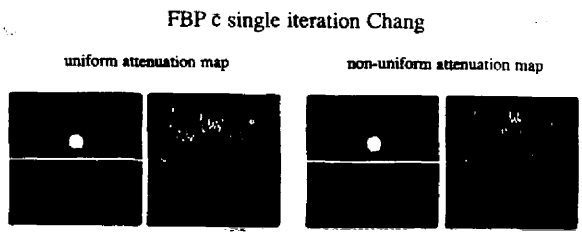


**FIGURE 4**
Results of FBP/Chang reconstruction for both uniform and nonuniform, broad-beam attenuation compensation. Profiles through the center of the images reveal improved quantitative accuracy and image quality with nonuniform compensation.

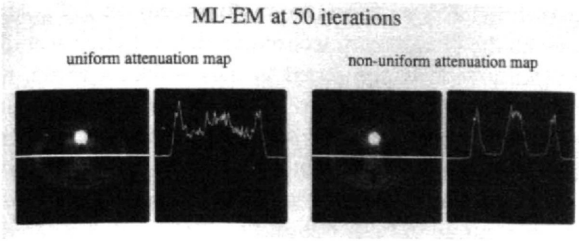


**FIGURE 5**
Results of ML-EM reconstruction for both uniform and nonuniform, broad-beam reconstruction. Improved quantitation and quality with nonuniform compensation is demonstrated with this algorithm.

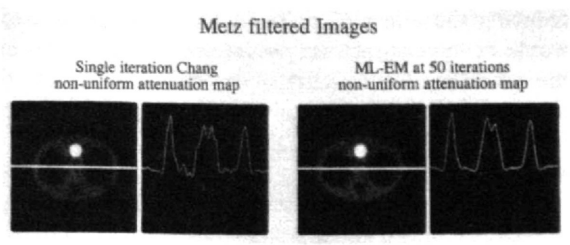


**FIGURE 7**
Metz filter results for both FBP/Chang and ML-EM. The greater noise with FBP/Chang and the overcompensation in the lungs with both algorithms are demonstrated.

iteration Chang with scatter subtraction, FBS in Table 2, had zero count density in the lung regions.) In spite of the fact that counts were subtracted from the projection data, the absolute count levels in the sphere and background regions were increased due to the narrow-beam attenuation compensation. Figure 6 shows reconstructions and profiles with both FBP/Chang and ML-EM with scatter subtraction.

When the Metz filter was applied to the reconstruction with broad-beam, nonuniform attenuation compensation, the result was a reduction in counts in the lungs areas and an increase in counts in the sphere and background regions. The quantitative accuracy in the sphere and background regions after Metz filtering was within 10%. This filter, in effect, redistributes the counts from the lungs into the other areas of the image and increases the contrast of the three regions. However, as can be seen in Table 2, the filter overcompensated in the sphere and lung regions. This overcompensation in the lung regions may be due to the decreased amount of scatter in the lungs relative to the background region. Altering the Metz filter formulation, either through the estimated MTF or the parameter X, can affect this overcompensation. Figure 7 shows the FBP/Chang and ML-EM reconstructions after Metz filtering. The figure illustrates the overcompensation in the lung regions and the smoother quality of the Metz filtered images as a result of the filter's suppression of high frequencies.

Table 2 also shows the relative noise magnitude measurements for each of the reconstruction methods including filtered backprojection. Within any individual compensation scheme, the ML-EM method had lower relative noise magnitude than FBP/Chang. This result is apparent in Figures 4–7 where the profiles through the FBP/Chang images show greater high frequency fluctuations relative to the ML-EM images. Noise in ML-EM images is iteration-dependent and so this result may be different at large iterations. Also, no attempt was made to control noise in the FBP/Chang images by smoothing. Within either the FBP/Chang or ML-EM method, the Metz filtered images had lowest noise followed by nonuniform and broad-beam, uniform and broad-beam, and finally scatter subtraction. Again, these results are illustrated in Figures 4–7.

The images in Figures 4–7 reveal artifacts of the reconstruction methods. For example, in both the FBP/Chang and ML-EM methods with uniform attenuation compensation, a dark band connects the top of the lungs with the hot sphere and distorts the shape of both the sphere and lungs. With either FBP/Chang or ML-EM, nonuniform attenuation compensation removes this band. Also, in the FBP/Chang images high intensity streaks can be observed emanating from the hot sphere especially with the scatter subtraction images. This could possibly be due to the amplification of the high frequency edges of the sphere by the ramp filter followed by backprojection. In the ML-EM images, these streaks are eliminated and the true shape of the sphere and lungs is reconstructed.

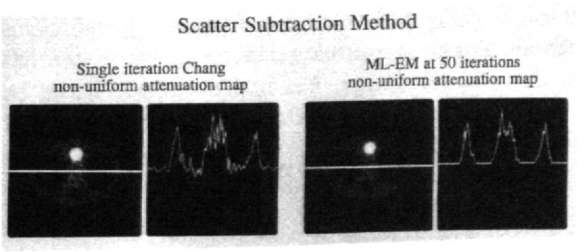


**FIGURE 6**
Scatter subtraction results for both FBP/Chang and ML-EM. The count level in the lung areas is close to zero with both algorithms.

## DISCUSSION

While nonuniform attenuation compensation offered a clear advantage over uniform compensation in this study, in practice it is difficult to obtain high quality transmission data for the attenuation map. While studies have demonstrated the feasibility of acquiring transmission data on commercial SPECT systems (*23*, *30*, *31*), the resulting attenuation maps are typically very noisy. The effect of this noise on lesion detection and quantitative accuracy in SPECT reconstructions has not been studied extensively. An interesting method of

reducing the effect of noise in the attenuation map would be to constrain the possible coefficient values in the transmission reconstruction based on a priori knowledge of tissue composition. This type of Bayesian reconstruction approach has been proposed for emission CT imaging (*32*).

The scatter subtraction technique used in this study improved contrast and quantitative accuracy compared with broad beam attenuation compensation. However, the accuracy of this technique is dependent on the selection of the scalar k. If one is to apply the scatter subtraction technique clinically, two important questions need addressing. First of all, how sensitive is k to changes in the source and attenuation distributions? The value for k found in this study, 0.4, is close to the value of 0.5 found by Jaszczak et al. (*25*), both for a cold sphere in a uniform circular phantom filled with $^{99m}$Tc solution and for a $^{99m}$Tc line source in the same phantom filled with water. These results suggest that k is not extremely sensitive to the source and attenuation distributions. Second, how sensitive is the accuracy of the reconstruction to error in k? In order to answer this question, the data used in this study were reconstructed using the FPB/Chang algorithm and the scatter subtraction technique with k equal to 0.5. The count levels in the sphere and background regions of the resulting reconstructed image were decreased by approximately 3% compared with the k = 0.4 image (FBS in Table 2). In this situation, therefore, a 25% error in k resulted in only a 3% incremental error in the reconstruction. This characteristic of scatter compensation has been noted previously by Jaszczak et al. (*33*).

A number of other issues should be considered before general application of the scatter subtraction technique. First, scatter subtraction results in increased noise in the reconstruction due to the decreased signal level and the propagation of the noise from the scatter data. For improved noise characteristics, it may be advantageous to apply a Metz filter to the data after scatter subtraction. In this case, the MTF of the filter need only contain the collimator response and not the scatter response. Second, subtraction violates the assumption of ML-EM that the data are Poisson random variables. As an alternative subtraction method for ML-EM, the photopeak and scatter data can be reconstructed separately and the subtraction performed after reconstruction. This would, however, double the computational time. Third, the scatter subtraction technique requires the capability of independent, dual-energy window acquisition. Fortunately, this capability is available in most commercial SPECT systems.

The use of broad-beam attenuation coefficients was investigated as a means of scatter compensation. This method was unable to eliminate counts in the lung areas of the reconstruction with either the FBP/Chang or ML-EM algorithms. This agrees with similar studies performed in a uniform attenuating medium (*25*). Although the broad-beam technique improves the overal quantitative level compared to narrow-beam alone, i does not accurately reconstruct quantitative levels in al regions of the image. The Metz filter was applied as a means of improving quantitative accuracy by deconvolving the scatter response. The resulting image was more accurate in both hot and cold regions compared with the broad-beam technique alone. The overcompensation observed in this study could be corrected through the selection of the filter power factor or MTF. Although the deconvolution technique is based on assumption of shift-invariance, the Metz filter may offer a practical alternative for scatter compensation.

Comparisons between the FBP/Chang and the ML-EM algorithm in terms of image noise depend to a large degree on the iteration stopping point for ML-EM and the filtering applied within either algorithm. Noise worsens with iteration with ML-EM, and although at 50 iterations ML-EM had better noise than FBP/Chang with the ramp filter, at higher iterations this may not be the case. However, since the quantitative accuracy of the ML-EM images at 50 iterations was at least as good as the FBP/Chang images, ML-EM may offer an advantage in the trade-off between noise and resolution/contrast. Important avenues of investigation in this area concern determining the optimal stopping point for ML-EM or stabilizing the algorithm so that deterioration with iteration does not occur.

## CONCLUSIONS

Of the compensation schemes evaluated in this study, the results suggest the most accurate method for either the FBP/Chang algorithm or the ML-EM algorithm is scatter compensation by either the subtraction technique or Metz filtering and nonuniform attenuation compensation. The results also suggest that the ML-EM algorithm can offer an advantage over FBP/Chang in the way of better image noise for the same degree of quantitative accuracy. Nonuniform attenuation compensation offers significant improvement in quantitative accuracy and reduces image artifacts compared with uniform compensation. Scatter compensation through the use of broad-beam attenuation coefficients cannot alone reconstruct accurate quantitative levels throughout the image, but improved results can be obtained when this method is combined with Metz filtering.

## ACKNOWLEDGMENT

This work was supported by Department of Energy Grant DE FG05 89ER 60894.

## REFERENCES


1. Sison JC, Shapiro B, Meyers L, et al. Metaiodobenzylguanidine to map scintigraphically the adrenergic nervous system in man. *J Nucl Med* 1987;28:1625–1636.
2. Drayer B, Jaszczak RJ, Friedman A, et al. In vivo quantitation of regional cerebral blood flow in glioma and cerebral infarction: validation of the HIPDM-SPECT method. *AJNR* 1983;4:572–576.
3. Budinger TF. Physical attributes of single photon tomography. *J Nucl Med* 1980;21:579–592.
4. Jaszczak RJ, Coleman RE, Whitehead FR. Physical factors affecting quantitative measurements using camera-based single photon emission computed tomography (SPECT). *IEEE Trans Nucl Sci* 1981;NS-28:69–80.
5. Hill TC, Holman BL, Lovett R. Initial experience with SPECT of the brain using N-isopropyl I-123-p-iodoamphetamine: concise communication. *J Nucl Med* 1982;23:191–195.
6. Holman BL, Hill TC, Magistretti PL. Brain imaging with ECT and radiolabeled amines. *Invest Radiol* 1982;17:206–215.
7. Kuhl DE, Barrio JR, Huang SC, et al. Quantifying local cerebral blood flow by N-isopropyl-p-[I-123]-iodoamphetamine (IMP) tomography. *J Nucl Med* 1982;23:196–203.
8. Coleman RE, Greer KL, Drayer BP, et al. Collimation for I-123 imaging with SPECT. In: Esser PD, ed. *Emission computed tomography—current trends.* New York: Society of Nuclear Medicine; 1983:135–145.
9. Polak JF, English RJ, Holman BL. Performance of collimators used for tomographic imaging I-123 contaminated with I-124. *J Nucl Med* 1983;24:1065–1069.
10. Polak JF, Holman BL, Moretti J, Eisner RL, Lister-James J, English RJ. I-123-HIPDM brain imaging with a rotating gamma camera and slant hole collimator. *J Nucl Med* 1984;25:495–498.
11. King MA, Schwinger RB, Penney BC, Doherty PW, Bianco JA. Digital restoration of indium-111 and iodine-123 SPECT images with optimized Metz filters. *J Nucl Med* 1986;27:1327–1336.
12. Macey DJ, DeNardo GL, DeNardo SJ, Hines HH. Comparison of low- and medium-energy collimators for SPECT imaging with iodine-123-labeled antibodies. *J Nucl Med* 1986;27:1467–1474.
13. Matsud H, Seki H, Sumiya H, et al. Quantitative cerebral blood flow measurements using N-isopropyl-(I-123)-p-iodoamphetamine and SPECT with a rotating camera. *Am J Physiol Imag* 1986;1:186–194.
14. Floyd CE, Jaszczak RJ, Greer IL, Coleman RE. Brain phantom: high resolution imaging with SPECT and I-123. *Radiology* 1987;164:279–281.
15. Thomas SR, Maxon HR, Keriakes JG, Saenger EL. Quantitative external counting techniques enabling improved diagnostic and therapeutic decisions in patients with well-differentiated thyroid cancer. *Radiology* 1977;122:731.
16. Chang L. A method for attenuation correction in radionuclide computed tomography. *IEEE Trans Nucl Sci* 1978NS-25:638–643.
17. Dempster AD, Laird NM, Rubin DB. Maximum likelihood from incomplete data via the EM algorithm. *J Royal Stat Soc* 1977;39:1–38.
18. Shepp LA, Vardi Y. Maximum likelihood reconstruction for emission tomography. *IEEE Trans Med Imag* 1982;MI-1:113–122.
19. Lange K, Carson R. EM reconstruction algorithms for emission and transmission tomography. *J Comp Assist Tomo* 1984;8:306–316.
20. Sorenson JA. Methods for quantitative measurement of radioactivity in vivo by whole-body counting. In: *Instrumentation in nuclear medicine, volume 2.* New York: Academic Press;1974:311–348.
21. Jaszczak RJ, Chang L, Stein NA, Moore FE. Whole-body single-photon emission computed tomography using dual large field-of-view scintillation cameras. *Phys Med Biol* 1979;24:1123–1143.
22. Manglos SH, Jaszczak RJ, Floyd CE, Hahn LJ, Greer KL, Coleman RE. Nonisotropic attenuation in SPECT: phantom tests of quantitative effects and compensation techniques. *J Nucl Med* 1987;28:1584–1591.
23. Tsui BMW, Gullberg GT, Edgerton ER, et al. Correction of nonuniform attenuation in cardiac SPECT imaging. *J Nucl Med* 1989;30:497–507.
24. Budinger TF, Gullberg GT. Three-dimensional reconstruction in nuclear medicine emission imaging. *IEEE Trans Nucl Sci* 1974;NS-21:2–20.
25. Jaszczak RJ, Greer KL, Floyd CE, Harris CC, Coleman RE. Improved SPECT quantification using compensation for scattered photons. *J Nucl Med* 1984;25:893–900.
26. Metz CE. A mathematical investigation of radioisotope scan image processing. Ph.D dissertation. University of Chicago, 1969.
27. Gullberg GT, Huesman RH, Malko JA, Pelc NJ, Budinger TF. An attenuated projector-backprojector for iterative SPECT reconstruction. *Phys Med Biol* 1985;30:799–815.
28. King MA, Schwinger RB, Penney BC. Variation of the count-dependent Metz filter with imaging system modulation transfer function. *Med Phys* 1986;13:139–149.
29. King MA, Penney BC, Glick SJ. An image-dependent Metz filter for nuclear medicine images. *J Nucl Med* 1988;29:1980–1989.
30. Malko JA, Van Heertum RL, Gullberg GT, Kowalsky WP. SPECT liver imaging using an iterative attenuation correction algorithm and an external flood source. *J Nucl Med* 1986;27:701–705.
31. Greer KL, Harris CC, Jaszczak RJ, et al. Transmission computed tomography data acquisition with a SPECT system. *J Nucl Med Technol* 1987;15:53–56.
32. Liang JZ, Jaszczak RJ, Coleman RE. Simultaneous reconstruction, segmentation, and edge enhancement of simulated heart images using a multinomial model and concentration-level information [Abstract]. *J Nucl Med* 1990;31:858.
33. Jaszczak RJ, Floyd CE, Coleman RE. Scatter compensation techniques for SPECT. *IEEE Trans Nucl Sci* 1985;NS-32:786–793.